Coseismic and Postseismic Deformation Estimation of the 2011 Tohoku Earthquake in Kanto Region, Japan, using InSAR Time Series Analysis and GPS

Tamer ElGharbawi and Masayuki Tamura

Department of civil and earth resources engineering, Kyoto university, Katsura, Nishikyoku, Kyoto, 615-8540, Japan.

Corresponding author:

Family name: ElGharbawi

First name: Tamer

Affiliation: Kyoto University, Kyoto, Japan

Address: Civil and Earth Resources Engineering, Kyoto University, Katsura, Nishikyoku, Kyoto, 615-8540, JAPAN

Tel: +81-90-6604-2014

E-mail: elgharbawi.mosaad.64z@st.kyoto-u.ac.jp

Abstract

We propose a methodology using interferometric synthetic aperture radar (InSAR) time series analysis and a single GPS station to estimate the coseismic and postseismic crustal deformations in the Kanto region, Japan, which has been affected by the 2011 Tohoku earthquake. The proposed methodology depends on choosing a proper deformation trend(s) to accurately describe the earthquake deformation signature by studying the deformation time series of a single GPS station. The modeled deformation trend is subtracted from the unwrapped phase maps to separate the main deformation signature from the imposed errors. Some deformation components, not described by the model(s), will leak to the residual phase maps which will be subjected to temporal and spatial filtering. The final corrected unwrapped phase maps are estimated by restoring the modeled deformation trend to the filtered residual phase maps and finally the deformation time series is estimated using a least squares technique. The proposed methodology was designed to retrieve complex and fine surface deformations in areas that have been affected by large dominating deformation signatures and contain at a least single GPS station. The methodology was tested using Envisat-ASAR C-band images and validation was carried out using GPS stations resulting in a mean RMS error of 6.9 millimeters. The estimated deformation time series shows a differential postseismic deformation pattern that can be attributed to an off Boso peninsula motion triggered by the 2011 Tohoku earthquake.

Keywords

2011 Tohoku Earthquake; Boso peninsula; Crustal Deformation Estimation; Coseismic; Postseismic; InSAR; GPS.

1. Introduction

Japan was struck by an M9.0 megathrust earthquake on March 11, 2011 at 05:46 Coordinated Universal Time (UTC). The 2011 Tohoku earthquake is the largest earthquake recorded in the history of seismic observation in Japan which affected the whole archipelago. Imakiire and Kobayashi (2011) presented the coseismic and postseismic displacement maps for Japan using the GNSS Earth Observation Network System (GEONET) (Yamagiwa et al., 2006). The coseismic crustal deformation was remarkably large with a maximum horizontal onshore movement of 5.3 meters and a subsidence of 1.2 meters. In addition to this large crustal motion, numerous researchers reported local surface deformations due to soil liquefaction and local subsidence in the Kanto region which caused significant damage to buildings and infrastructure (Bhattacharya et al., 2011; Yamaguchi et al., 2012; Yasuda et al., 2012; Tokimatsu et al., 2012; Tsukamoto et al., 2012; Ishihara, 2012).

The Kanto region is located above the complex intersection of two subducting plates: the Pacific plate which is subducting beneath the Okhotsk plate from the east, and the Philippine Sea plate, which is subducting beneath the Okhotsk plate from the southeast (Fig. 1.a) (Somerville, 2014), and with an unprecedented earthquake of that magnitude, the need for monitoring the postseismic crustal deformations with fine spatial resolution has been raised. Interferometric synthetic aperture radar (InSAR) has been used successfully to measure and study surface deformation due to several phenomena (Burgmann et al., 2000) such as glacier movements (Goldstein et al., 1993), earthquakes (Massonnet et al., 1994), land subsidence (Buckley et al., 2003) and interseismic deformations along faults (Wright et al., 2004; Biggs et al., 2007; Gourmelen et al., 2010). However, InSAR is strongly affected by atmospheric variations such as tropospheric and ionospheric delays. The quality of InSAR measurements is also affected by the quality of satellite orbital data which can be identified as additional long wave interferometric fringes.

Several researchers have presented valuable methods for InSAR stacking and time series analysis that can produce an accurate deformation time series. Sandwell and Price (1998) presented InSAR stacking using a phase gradient approach to construct averages of interferograms without phase unwrapping to increase fringe clarity and decrease errors. Berardino et al. (2002) presented the Small Baseline Subset (SBAS) approach which uses a singular value decomposition (SVD) to link disconnected SAR acquisition subsets. Schmidt and Burgmann (2003) used a least squares inversion of differential interferograms to estimate the incremental range change between SAR acquisitions. They stated that a minimum number of 30 interferograms is required to produce a reasonable time series.

Other researchers presented and established improvements that can be obtained by integrating InSAR and GPS observables. Samsonov et al. (2007) modeled the deformation velocities of southern California using 140 GPS stations. They used the modeled velocity maps and the mean velocity maps estimated from InSAR stacking to minimize an energy function to find the most probable values for deformation velocities in three dimensions. Wei et al. (2010) created a vector velocity model based on GPS and removed it from the interferograms then filtered the phase residuals and restored the vector velocity model in a technique they called Remove/Filter/Restore. Tong et al. (2013) integrated InSAR and GPS observations using a Sum/Remove/Filter/Restore approach to evaluate creep rates along major faults of the San Andreas Fault.

The deformation signature of the 2011 Tohoku earthquake was remarkable and unprecedented. It can be categorized into two major components; first, the coseismic deformation, which includes the major shift of the whole archipelago and the local deformations caused by soil liquefactions and local land subsidence. The second component is the postseismic crustal deformation which has been ongoing around the Tohoku and Kanto regions for several months after the main shock (Imakiire and Kobayashi, 2011). The major shift is demonstrated in InSAR as long wavelength patterns that dominate the entire deformation maps leaving no stable zones for adequate calibration and correction. These long wavelength patterns arevery similar to orbital error effects and long wavelength patterns of the atmosphere, making the imposed errors and the actual deformation really challenging to distinguish. Several researches presented valuable analyses for the coseismic crustal deformations of the 2011 Tohoku earthquake. Martinez et al. (2012) used TerraSAR-X image correlation to produce ground displacement maps. They quantitatively compared their results with GPS data which showed a divergence of about 15 cm. Feng et al. (2012) used entire strips of ALOS-PALSAR and ENVISAT-ASAR images combined with GPS observations to present crustal deformation maps. They validated their results using GPS measurements showing accuracy (RMS) of 7.7 cm. ElGharbawi and Tamura (2014) used ALOS-PALSAR and GPS observation for the Tokyo bay area to produce coseismic deformation maps. They used GPS observations to model and correct the tropospheric delay, then applied a GPS based supervised spatial phase filtering to identify the deformation signature. They validated their results against GPS showing an accuracy of 0.56 cm.

The focus of this paper is estimating the coseismic and postseismic crustal deformation in the Kanto region, which was affected by the 2011 Tohoku earthquake. During data analysis, several challenges were identified. First is the small number of available coseismic and postseismic SAR acquisitions, preventing an adequate application of SBAS and least squares inversion methods because these methods need at least 30 interferograms with a small normal baseline (nearly 20% of the critical normal baseline) (Schmidt and Burgmann, 2003). Second, the dominating deformation signature of the 2011 Tohoku Earthquake made the identification of long wavelength patterns of imposed errors, such as baseline error, challenging. In addition, any phase filtering method will contaminate the deformation signature if applied directly to the unwrapped phase maps. To clarify this limitation, we can subdivide the deformation patterns into three categories. First, long wavelength signatures will be affected or even totally removed if the orbital correction or ramp removal for filtering is applied. Second, local deformation will be contaminated if we use a spatial low pass filter to reduce tropospheric effects. Finally, the temporal trend of the deformation, with high and low temporal frequencies, will prevent adequate application of temporal filtering methods.

In this paper, we propose a methodology that can produce deformation time series with geodetic accuracy for our study area using a small number of SAR acquisitions and a single GPS station. The main motivation of this analysis is the need for estimating the full deformation signature, i.e., the long and short wavelength components, of the study area using a limited number of SAR acquisitions. The basic idea of this approach is simulating the time series deformation using as many models as needed. The proper deformation trend(s) is identified by studying the time series deformation from a sample GPS station. The trends' parameters are estimated by the least squares approach using the raw unwrapped phase maps. The modeled deformation should identify the dominant deformation patterns; this leaves local deformation and other imposed errors that can be separated easily. A comprehensive description of the methodology can be presented as follows. (1) We generate the required unwrapped phase maps using the available SAR acquisitions. Then, we use a single GPS station as a reference point to register the unwrapped phase maps. (2) We use the GPS station observations to identify the best deformation trend(s) that fits the deformation time series. (3) We use a least squares inversion to estimate the parameters of the deformation trends' in the study area using the raw unwrapped phase maps. (4) Using the trends' parameters, we estimate the deformation maps for every raw unwrapped phase map, and then subtract this model from the unwrapped phase maps to generate the residual phase maps. (5) For the residual phase maps, we apply temporal phase filtering using least squares and spatial ramp removal. (6) Finally, we restore the modeled deformation trend to the filtered phase residuals and estimate the deformation maps using least squares analysis.

In this proposed methodology, we estimate the deformation parameters without any dependency on the GPS observations, with the exception of identifying deformation trends' mathematical expressions and the unwrapped phase map registration. Additionally, all of the filtering processes were implemented on the residual phase maps, which preserve the main deformation signature. In addition, we introduce deformation signature estimation using a multi-model analysis, which was necessary because of the large magnitude of main earthquake shock. This large shock makes deformation estimation using the mean velocity or single deformation trend meaningless and unrealistic. We believe that this method can be utilized to study complex and fine-scale surface deformation in areas that been affected by large dominating deformation signatures and contain at least a single GPS station.

This paper is organized as follows: Section 2 describes the study area and data used. Section 3 presents the proposed methodology. Section 4 presents the application of the proposed methodology to the Kanto region. Section 5 presents a discussion on the deformation signature based on the presented analysis, and finally, section 6 is dedicated to conclusions.

2. Study Area and Data Used

2.1 Study Area and 2011 Tohoku Earthquake

In this analysis, we studied the deformation in part of the Kanto region that contains the Tokyo bay area and is located above a complex intersection of tectonic plates (Fig. 1.a). The area under study is nearly 70 km by 75 km and contains urban and vegetated areas. This region was heavily affected by the M9.0 megathrust 2011 Tohoku earthquake that struck Japan on March 11, 2011 at 05:46 (UTC). For better demonstration of the challenges in this analysis, we present in Fig. 2 the coseismic and postseismic interferograms, which demonstrate the severity of crustal deformation in our study area. The deformation signature can be subcategorized into three types; first, the large coseismic deformation or shift that affected the entire region (Fig. 2.a), second, the local deformation that occurred as a result of this large motion, such as local subsidence and soil liquefaction, and third, the postseismic crustal deformation (Fig. 2.b, 2.c and 2.d). In this analysis, we present time series deformation maps for the study area that illustrate the coseismic and postseismic crustal deformation, along with a detailed discussion of the different signatures presented in deformation maps.

2.2 Data Used

We use Synthetic Aperture Radar (SAR) images and GPS observations to monitor crustal deformation in our study area. SAR images were provided by the European Space Agency © ESA (2014). The images were acquired by ESA's satellite ENVISAT-ASAR. Six C-band SAR images for the Kanto region, Japan were obtained using Image Single polarization (HH) mode in descending direction (see table 1). One of the major challenges in our analysis was the limited postseismic SAR acquisitions, primarily as a result of the termination of ENVISAT-ASAR mission shortly after the 2011 Tohoku earthquake.

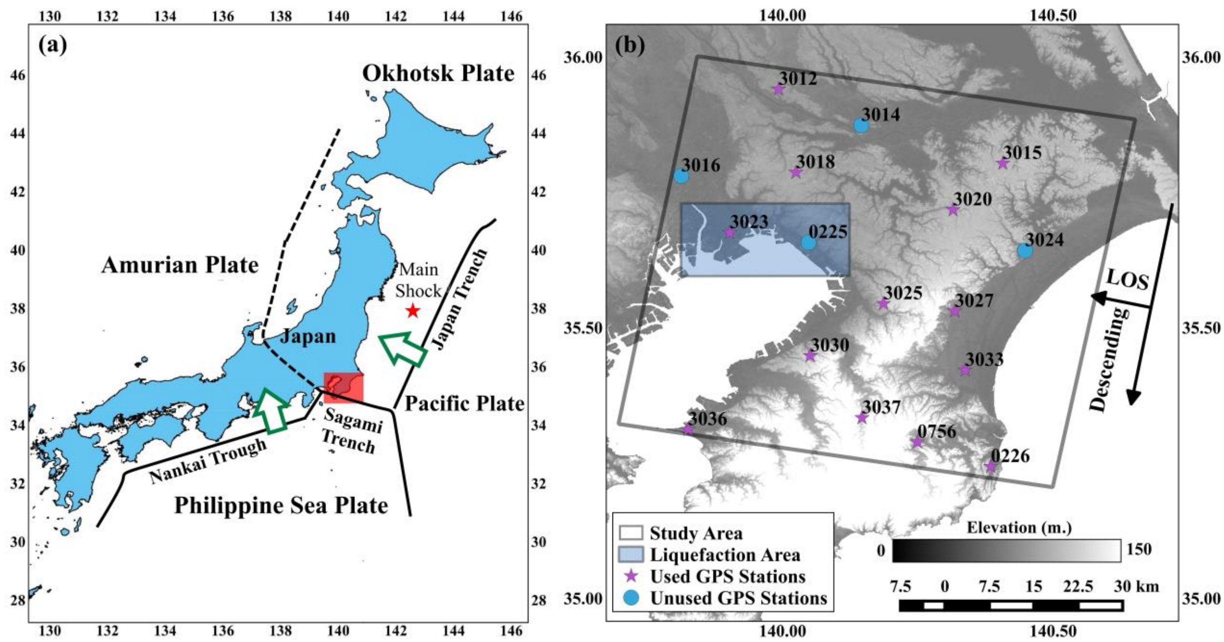

Fig.1. (a) Japan map showing study area location and tectonic plates boundries , (b) Study area showing GPS stations, small rectangle identifies areas that heavily affected by soil liquefaction..

The GPS observations were obtained from Japan's permanent nationwide GPS array GEONET, which was established by the Geospatial Information Authority of Japan (GSI) to monitor crustal deformation and provide reference coordinates for land surveying by GPS. They cover the whole area of Japan with more than 1200 permanent GPS stations. The mean distance between stations is approximately 25 km (Yamagiwa et al., 2006). One of GEONET's products is the corrected coordinates of GPS stations nationwide. For every GPS station, GEONET provides one file containing the daily value of the corrected coordinate for the entire year. GEONET uses ITRF2005 as a reference coordinate frame and GRS-80 as a reference ellipsoid.

The GPS stations used in this analysis are presented in Fig. 1.b. We used the GPS stations located within study area boundaries (Fig. 1.b, "Used GPS Stations") to validate the accuracy of the proposed methodology. During the InSAR analysis, deformation values for some pixels could not be estimated due to severe de-correlation effects; for that reason, some GPS stations were not used in the validation process (Fig. 1.b, “Unused GPS Stations”).

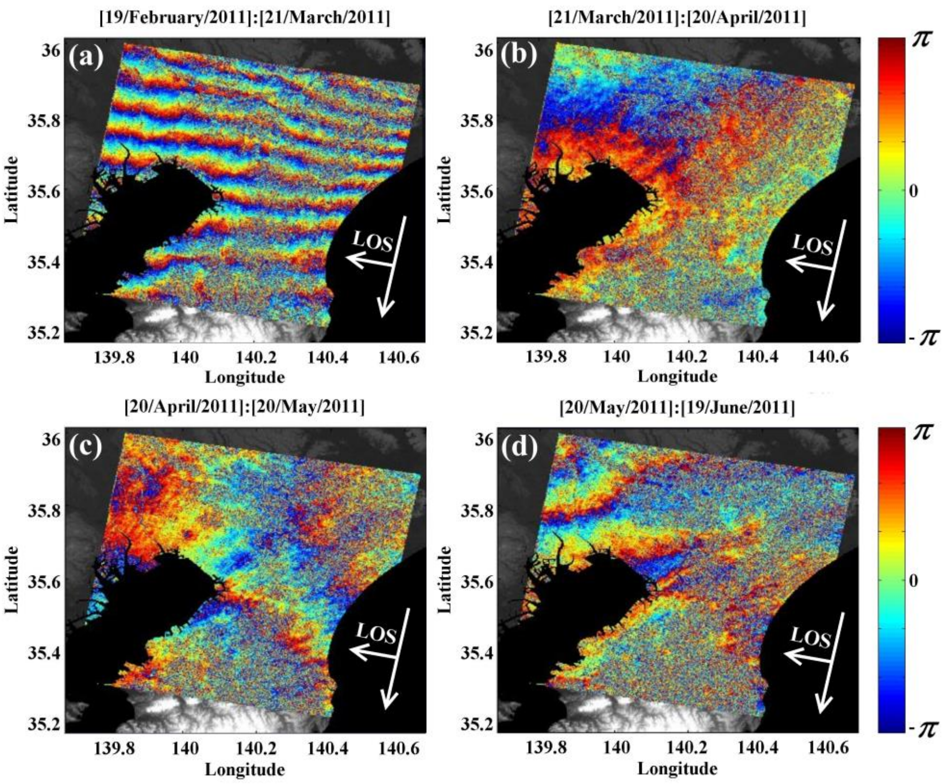

Fig.2. Interferograms using ENVISAT-ASAR C-band images, each fringe cycle equevalent to a displacement of 2.8 cm. (a) coseismic interferogram [19/Feb/2011 : 21/March/2011], and postseismic interferograms (b) [21/March/2011 : 20/April/2011], (c) [20/April/2011 : 20/May/2011], (d) [20/May/2011 : 19/June/2011], background is a DEM map.

3. Methodology

This section describes the proposed methodology in detail. The general block diagram of the analysis steps is illustrated in Fig. 3.

3.1 InSAR Analysis

The interferogram phase is generated using two single look complex (SLC) images, presented in eq. (1), where ϕ_{Topo}^{Res} is the residual topographic component after removal of topography effects using a Digital Elevation Model (DEM). In this research, we used the Shuttle Radar Topography Mission (SRTM-3) DEM to remove the topography effects presented in interferograms. The interferometric phase also contains deformation effects, ϕ_{Deform}, atmospheric delay effects, ϕ_{Atm}, baseline error effects, $\phi_{Baseline}$ and noise effects, ϕ_{Noise}.

$$\phi_{InSAR} = \phi_{Topo}^{Res} + \phi_{Deform} + \phi_{Atm} + \phi_{Baseline} + \phi_{Noise} \quad (1)$$

The rationale of the proposed methodology assumes that the imposed errors, mainly (ϕ_{Atm} , $\phi_{Baseline}$), in the interferometric phase are spatially correlated and temporally obey Gaussian distribution. Under this assumption, the temporal component of the imposed errors can be effectively reduced using a least squares method and the spatial component can be removed using the spatial ramp removal algorithm, e.g., Zhang et al. (2004). The primary challenge in this analysis is the large deformation signature that dominates the entire study region and that has the same characteristics of other long wavelength imposed errors, such as baseline error. In this case, the application of ramp removal or filtering of the raw unwrapped phase maps would contaminate the deformation signature and produce large errors in the final deformation maps. For that reason, our main focus is to model the deformation time series signature and remove it from the raw observations and then apply filtering processes to the residual phase maps. After filtering, we restore the modeled deformation trend and a final deformation estimation process is implemented.

Let us consider that the number of available SAR images for the same area equals N and are ordered in a time series [t_1: t_N]. Then, the number of the unknown deformations for each pixel will equal $n = N\text{-}1$ and can be identified by [d_1: d_n]. The maximum number of differential interferograms is $M = N!/((N-2)!\,2!)$.

After interferogram generation, flattening, filtering and phase unwrapping (Fig. 3, Step A) are performed. The unwrapped phase maps must be registered or referenced to a pixel with known deformation value; because there are no stable zones in the study region, we use GPS station no. 3025 (Fig. 1.b) as a reference point for registering the unwrapped phase maps.

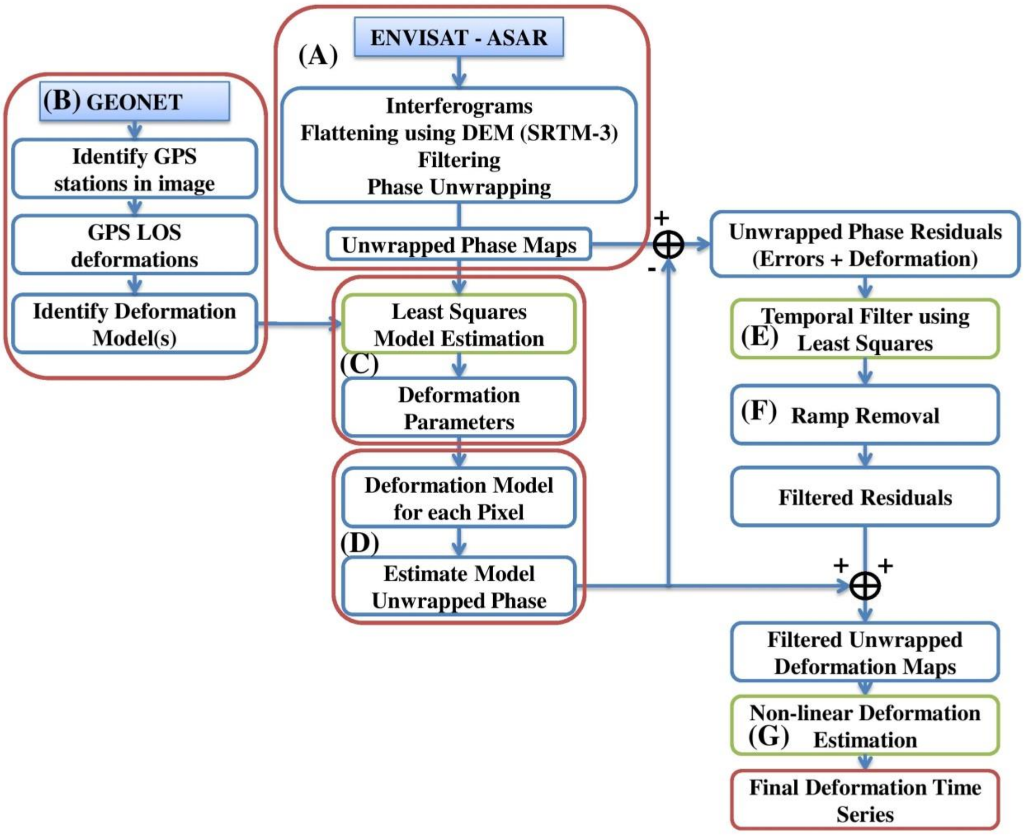

Fig.3. Methodology block diagram

3.2 Deformation Trend Estimation

Using GPS network observations to model earthquake deformation we generate significant errors during interpolation, even when using a dense GPS network such as GEONET. In addition, the availability of a dense GPS network can be very challenging for many sites around the world. For these reasons, we are proposing to describe the deformation time series signature by several consecutive deformation trends (Fig. 3, Step B). The mathematical expressions of these trends can be identified using observations of a single GPS station. Then, the trends' parameters are estimated for each pixel using the unwrapped phase stack.

We used GPS station no. 3025 (Fig. 1.b) to study the deformation time series signature and identify the best mathematical expressions to represent it. As illustrated in Fig. 4, the deformation trends before and after the earthquake are completely different; therefore, we divided it into two parts. Before the earthquake, the best mathematical expression that fits the signature is the linear model $d = a \cdot t$, where d is the deformation value, a is an unknown deformation parameter and t is the time value in days. After the earthquake, the best mathematical expression that fits this part is the power model $d = b \cdot T^c$, where $b \; and \; c$ are unknown deformation parameters and T is the time value in days starting at the earthquake. We have to separate the time axis to describe the deformation signature adequately because the power function will go to infinity when $T = 0$, accurately representing the sudden shock of the earthquake.

In this analysis, we use two models to describe the deformation time series. The second model was a non-linear power model, which forces the use of an iterative non-linear least squares approach to estimate the three parameters of the two chosen models. It should be noted that for more complex deformation patterns, more models could be added to the system for better simulation of the deformation. On the other hand, increasing the number of parameters will require more data (unwrapped phase maps) for better estimation.

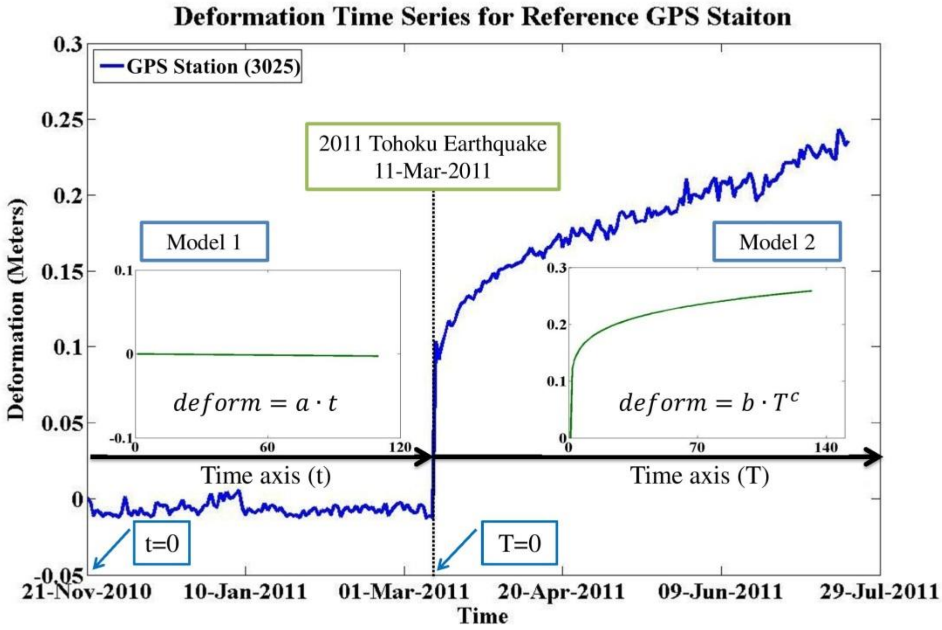

Fig.4. Observed LOS deformation using GPS station no. 3025 and the proposed deformation trends.

3.3 Modeling Deformation

After identifying the best deformation trend(s), we use the unwrapped phase stack to estimate the trends' parameters using the least squares method. Then, we use the estimated parameters to generate deformation trend maps with the same structure and number as the raw unwrapped phase maps. Afterwards, we subtract each modeled deformation map from its equivalent unwrapped phase map to generate the residual maps that will be filtered using the method described below.

3.3.1 Model Parameter Estimation

After phase unwrapping and model identification, the unknown model parameters $\boldsymbol{P}^{\boldsymbol{T}}$ = [a, b, c] are estimated for each pixel by minimizing the squared error function (***E***) eq. (2) (Fig. 3, Step C).

$$\boldsymbol{E} = \sum_{i=1}^{M} \left(LOS_i - D_i^m - \Delta\, Topo_i\right)^2 \Rightarrow minimum \qquad (2.a)$$

$$D_i^m = a \cdot \left({t^i}_{slave} - {t^i}_{master}\right) + b \cdot \left(\left({T^i}_{slave}\right)^c - \left({T^i}_{master}\right)^c\right) \qquad (2.b)$$

$$\Delta\, Topo_i = \left(B_{\perp i} \cdot \delta h\right)/\left(r_i \cdot sin\, \vartheta_i\right) \qquad (2.c)$$

where LOS_i is the i^{th} InSAR line-of-sight deformation, D_i^m is the modeled deformation value, $\Delta\, Topo_i$ is the topography error, $B_{\perp i}$ is the normal baseline, δh is the DEM error, r_i is the sensor target distance and ϑ_i is the incident angle; the subscript (i) refers to the i^{th} interfero-gram.

The system is non-linear. Therefore, we need to linearize it first by expanding the equation using Taylor series and use only the linear terms of eq. (3).

$$f(a, b, c, \delta h) = f(a_o, b_o, c_o, \delta h_o) + f(\Delta a, \Delta b, \Delta c, \Delta\delta h) \qquad (3.a)$$

$$f(\Delta a, \Delta b, \Delta c, \Delta\delta h) = \frac{\partial f(a,b,c,\delta h)}{\partial a}\, \Delta a + \frac{\partial f(a,b,c,\delta h)}{\partial b}\, \Delta b + \frac{\partial f(a,b,c,\delta h)}{\partial c}\, \Delta c + \frac{\partial f(a,b,c,\delta h)}{\partial \delta h}\, \Delta\delta h$$

(3.b)

$$\frac{\partial f(a,b,c,\delta h)}{\partial a} = t_{slave} - t_{master} \qquad (3.c)$$

$$\frac{\partial f(a,b,c,\delta h)}{\partial b} = (T_{slave})^c - (T_{master})^c \qquad (3.d)$$

$$\frac{\partial f(a,b,c,\delta h)}{\partial c} = (b \cdot (T_{slave})^c) \cdot \ln(T_{slave}) - (b \cdot (T_{master})^c) \cdot \ln(T_{master}) \quad (3.e)$$

$$\frac{\partial f(a,b,c,\delta h)}{\partial \delta h} = (B_{\perp i})/(r_i \cdot sin\,\vartheta_i) \quad (3.f)$$

By assuming prior values for $(a_o, b_o, c_o, \delta h_o)$, we can solve for $(\Delta a, \Delta b, \Delta c, \Delta\delta h)$ by iterative least squares analysis eq. (4). The prior values are chosen based on the analysis of the sample GPS station deformation trend, except for δh_o, which is assumed to be zero.

$$\boldsymbol{U} = \left(\boldsymbol{A_m^T} \cdot \boldsymbol{A_m}\right)^{-\boldsymbol{1}} \cdot (\boldsymbol{A_m^T} \cdot \boldsymbol{L}) \quad (4)$$

where:

$$\boldsymbol{A_m} = \begin{bmatrix} \frac{\partial f^1}{\partial a} & \frac{\partial f^1}{\partial b} & \frac{\partial f^1}{\partial c} & \frac{\partial f^1}{\partial \delta h} \\ \vdots & \vdots & \vdots & \vdots \\ \frac{\partial f^M}{\partial a} & \frac{\partial f^M}{\partial b} & \frac{\partial f^M}{\partial c} & \frac{\partial f^M}{\partial \delta h} \end{bmatrix}, \boldsymbol{U} = \begin{bmatrix} \Delta a \\ \Delta b \\ \Delta c \\ \Delta\delta h \end{bmatrix}, \boldsymbol{L} = \begin{bmatrix} LOS_1 \\ \vdots \\ LOS_M \end{bmatrix} \; and \; \boldsymbol{P} = \begin{bmatrix} a_o \\ b_o \\ c_o \\ \delta h_o \end{bmatrix} + \begin{bmatrix} \Delta a \\ \Delta b \\ \Delta c \\ \Delta\delta h \end{bmatrix}$$

The system converges, and a solution is reached when $\boldsymbol{U}$ is nearly zero. In this analysis step, we use only the pixels that exhibit coherence values higher than the coherence threshold value for the entire unwrapped phase stack. This will result in low spatial coverage of the estimated parameters; therefore, after the parameter estimation process, we use a 7-pixels-by-7-pixels moving window to interpolate the three parameters in the pixels that fell below the coherence threshold and have coherent neighboring pixels within the 7-by-7 window. To accelerate the interpolation process, we use the average value of the moving window for the unestimated pixels only. It should be noted that, if the pixel phase is subject to large errors, sometimes the solution will not converge for that pixel. In that case, the pixel is neglected, and if it has reliable neighboring pixels, it will be estimated during the parameter interpolation process. Taking the DEM error (δh) into consideration during the parameter estimation process makes the system easier to converge. Nevertheless, we did not correct the input data for DEM error (δh) during the analysis; we left it to be finally estimated in the last processing step along with the final deformation values.

3.3.2 Deformation Map Model

The main idea of the methodology is to apply the filtering and correction processes on the observed data, not on the estimated deformation, to avoid any additional errors generated during deformation modeling. Therefore, after estimating the deformation parameters for each pixel, we calculate the deformation values at the acquisition time of every SAR image and generate deformation trend maps with the same structure and number of the raw unwrapped phase maps (Fig. 3, Step D). Then, by subtracting each deformation trend map from its equivalent unwrapped phase maps, the residual phase maps are generated. These residual phase maps contain part of the deformation signature that cannot be represented by the model, in addition to the imposed errors eq. (5).

$$\phi_{Res} = \phi_{Topo}^{Res} + \phi_{Deform}^{Res} + \phi_{Atm} + \phi_{Baseline} + \phi_{Noise} \quad (5)$$

Finally, filtering is performed on the residual maps to extract the residual deformation signature and eliminate the imposed errors.

3.4 Residual Filtering

3.4.1 Temporal Filtering

In our study, we assume that the imposed errors temporally obey a Gaussian distribution; therefore, errors can be effectively reduced using a least squares method (Fig. 3, Step E). In our analysis, we use six SAR images, the smallest number to effectively reduce the temporal errors using least squares. Therefore, we generated 15 interferograms using all of the possible combinations without using a perpendicular baseline threshold other than the critical one (see table 1). The imposed errors are reduced significantly using this number of interferograms and by applying the temporal filtering to the residual phases. However, we do not think that this approach can effectively reduce the temporal errors using less number of SAR images.

The main idea in our analysis is to correct the original raw unwrapped phase maps first. Afterwards, we estimate the deformation time series using the corrected unwrapped phase maps. For that reason, in this filtering step, we are interested in correcting the residual phase maps (ϕ_{Res}) rather than estimating the residual deformations **(dr)**. After residual phase estimation, the residual deformations $\boldsymbol{dr}$ = [dr_1 : dr_n] are estimated by minimizing the squared error function **($\boldsymbol{E1}$)** eq. (6), eq. (7) .

$$\boldsymbol{E1} = \sum_{i=1}^{M}\left(LOS_i^{Res} - Dr_i - \Delta\, Topo_i\right)^2 \Rightarrow minimum \quad (6.a)$$

$$Dr_i = \sum_{\mathrm{j=t}(Master)}^{\mathrm{t}(Slave)} dr_j \quad (6.b)$$

where LOS_i^{Res} is the i^{th} InSAR line-of-sight residual deformation, Dr_i is the unknown residual deformation components for the i^{th} interferogram and dr_j is the unknown residual deformation of time segment j. The minimum value of the squared error function $\boldsymbol{E1}$ is reached when the first derivatives with respect to each component of the unknown surface deformations (dr_j**)** are zero. This gives rise to the linear equation presented in eq. (7.a).

$$\boldsymbol{Ur} = \left(\boldsymbol{A_r}^{\mathbf{T}} \cdot \boldsymbol{A_r}\right)^{-\mathbf{1}} \cdot \left(\boldsymbol{A_r}^{\mathbf{T}} \cdot \boldsymbol{L_r}\right) \quad (7.a)$$

where:

$$\boldsymbol{B_r} = \begin{bmatrix} \frac{\partial Dr_1}{\partial dr_1} & \cdots & \frac{\partial Dr_1}{\partial dr_n} \\ \vdots & \ddots & \cdots \\ \frac{\partial Dr_M}{\partial dr_1} & \cdots & \frac{\partial Dr_M}{\partial dr_n} \end{bmatrix}_{M \times n}, \boldsymbol{L_r} = \begin{bmatrix} LOS_1^{Res} \\ \vdots \\ LOS_M^{Res} \end{bmatrix} \; and \;\; \boldsymbol{Ur} = \begin{bmatrix} dr_1 \\ \vdots \\ dr_n \\ \delta h \end{bmatrix}$$

The design matrix $\boldsymbol{A_r}$ has dimensions of $M \times (n+1)$, where $\boldsymbol{A_r} = [\boldsymbol{B_r}, \boldsymbol{c}]$, $\boldsymbol{B_r}$ is the partial derivative of Dr_i with respect to dr_j, $\boldsymbol{c^T} = [(B_{\perp 1})/(r_1 \cdot sin\,\vartheta_1), \cdots, (B_{\perp M})/(r_M \cdot sin\,\vartheta_M)\,]$, $\boldsymbol{Ur}$ is the unknown vector with dimensions $(n+1) \times 1$ and $\boldsymbol{L_r}$ is the residual LOS deformation vector with dimensions $M \times 1$. The matrix $\boldsymbol{A_r}^{\mathbf{T}} \cdot \boldsymbol{A_r}$ is a non-singular matrix; therefore, inverting this linear system should be simple. If the pixel's coherence is under the threshold in few observations, the system can be solved, but sometimes the matrix $\boldsymbol{A_r}^{\mathbf{T}} \cdot \boldsymbol{A_r}$ can become singular. In that case we use the singular value decomposition (SVD) to invert the system. The temporal filtered residual phase $\phi_{Res}^{Temp.Filter}$ is estimated by eq. (7.b).

$$\phi_{Res}^{Temp.Filter} = \boldsymbol{Ar} \cdot \boldsymbol{Ur} = \phi_{Topo}^{Res} + \phi_{Deform}^{Res} + \phi_{Atm}^{Spatial\ comp.} + \phi_{Baseline}^{Spatial\ comp.} + \phi_{Noise} \quad (7.b)$$

3.4.2 Spatial Filtering

After correcting the residual phase maps temporally $\phi_{Res}^{Temp.Filter}$, spatially correlated errors such as baseline errors and long wavelength atmospheric signatures are still presented. The best way to remove such errors is by ramp removal (Fig. 3, Step F). This filtering method would contaminate the deformation signature if applied directly to the raw unwrapped phase maps, but after separating the main deformation signature it can be applied safely to the residual phase maps. We chose to fit a first degree surface in both directions to every residual phase map then remove this surface from it. This process will remove the spatially correlated errors in the residual unwrapped phase maps $\phi_{Res}^{Temp.Filter}$ and produce the final filtered residual phase maps $\phi_{Res}^{Final\ Filter}$. After this step, the deformation trend maps are restored to the filtered residual phase maps to generate the final filtered unwrapped phase maps that will be used in estimating the final deformation time series.

3.5 Final Deformation Estimation

Restoring the deformation trend to the filtered residual phase maps generates the corrected unwrapped phase maps. These maps are used in estimating the incremental LOS deformation time series by least squares method (Fig. 3, Step G). The proposed stacking structure will generate a non-singular matrix system ($\mathbf{A^T \cdot A}$) if the pixel's coherence is above the threshold in the entire stack. On the other hand, this condition will limit the spatial coverage of the estimated deformation map. For that reason, we can use pixels that fall below the coherence threshold in a few unwrapped phase maps providing that every deformation segment [d_1: d_n] is adequately presented in the unwrapped phase stack. This slight modification can make the matrix system singular, mainly because of the small number of available SAR images. In that case, the SVD can be used to invert the system, but that can produce unrealistic deformation values because the SVD adopts the minimum norm solution. This problem was presented and solved by Berardino et al. (2002). They proposed to solve for deformation velocities rather than deformation values. This solution (SBAS) will present realistic deformation values. An additional integration step is needed to convert velocity values to time series deformation.

The unknown deformations velocities $\boldsymbol{V} = [V_1 : V_n]$ are estimated by minimizing the squared error function ($\boldsymbol{E2}$) eq. (8).

$$\boldsymbol{E2} = \sum_{i=1}^{M} \left(LOS_i - D_i - \Delta\, Topo_i\right)^2 \Rightarrow minimum \qquad (8.a)$$

$$D_i = \sum_{j=t(Master)}^{t(Slave)} (\Delta t_j)\, V_j \qquad (8.b)$$

where LOS_i is the i^{th} InSAR LOS deformation, D_i is the unknown deformation components for the i^{th} interferogram and V_j is the unknown velocity of time segment j. The minimum value of the squared error function $\boldsymbol{E2}$ is reached when the first derivatives with respect to each component of the unknown surface deformations velocity (V_j) are zero. This gives rise to the linear equation presented in eq. (9).

$$\boldsymbol{V} = (\boldsymbol{A}^{\boldsymbol{T}} \cdot \boldsymbol{A})^{-\boldsymbol{1}} \cdot (\boldsymbol{A}^{\boldsymbol{T}} \cdot \boldsymbol{L}) \qquad (9)$$

where $\boldsymbol{A}$ is a design matrix with dimensions $M \times (n+1)$, $\boldsymbol{V}$ is the unknown velocity vector with dimensions $(n+1) \times 1$ and $\boldsymbol{L}$ is the observed LOS deformation vector with dimensions $M \times 1$.

The design matrix $\boldsymbol{A} = [\boldsymbol{B}, \mathbf{c}]$ and unknown velocity vector of the system is $\boldsymbol{V}^{\boldsymbol{T}} = [V_1, \cdots, V_n, \delta h]$, where $\boldsymbol{B}$ is the partial derivative of D_i with respect to V_j eq. (10) and $\boldsymbol{c}^{\boldsymbol{T}} = [(B_{\perp 1})/(r_1 \cdot sin\, \vartheta_1), \cdots, (B_{\perp M})/(r_M \cdot sin\, \vartheta_M)]$.

$$\boldsymbol{B} = \begin{bmatrix} \frac{\partial D^1}{\partial V_1} & \cdots & \frac{\partial D^1}{\partial V_j} \\ \vdots & \ddots & \vdots \\ \frac{\partial D^M}{\partial V_1} & \cdots & \frac{\partial D^M}{\partial V_j} \end{bmatrix} \qquad (10)$$

4. Analysis and Results

In this analysis, we use six SAR images, which were acquired by ENVISAT-ASAR and cover the period from 21 November 2010 to 19 June 2011. Data were provided by the European Space Agency (2014).

4.1 Data Preparation

Six C-band SAR images for the Kanto region, Japan, were obtained from ESA's ENVISAT-ASAR using Image Single polarization (HH) mode in descending direction (see table 1). Corrected coordinates estimated at GEONETs' GPS stations were used for registering the unwrapped phase maps, determining the deformation trend(s) and accuracy verification of the final results. Seventeen GPS stations within the image were identified (Fig. 1.b). Interferograms were generated using SARscape software as shown in (Fig. 5) and (Table 1). We use SRTM-3 DEM to remove the effect of topography, Goldstein method (Goldstein and Werner, 1998) for filtering and Delaney Minimum Cost Flow (DMCF) (Costanthi and Rosen, 1999) for phase unwrapping with coherence threshold of 0.2. To reduce the effect of phase decorrelation, we use multilooking of one look in range and five looks in azimuth. Unwrapped phase maps were converted to displacements using eq. (11).

$$\Delta = -1 * \frac{\phi \times \lambda}{4 \pi} \quad (11)$$

where λ is the wavelength and ϕ is the unwrapped phase.

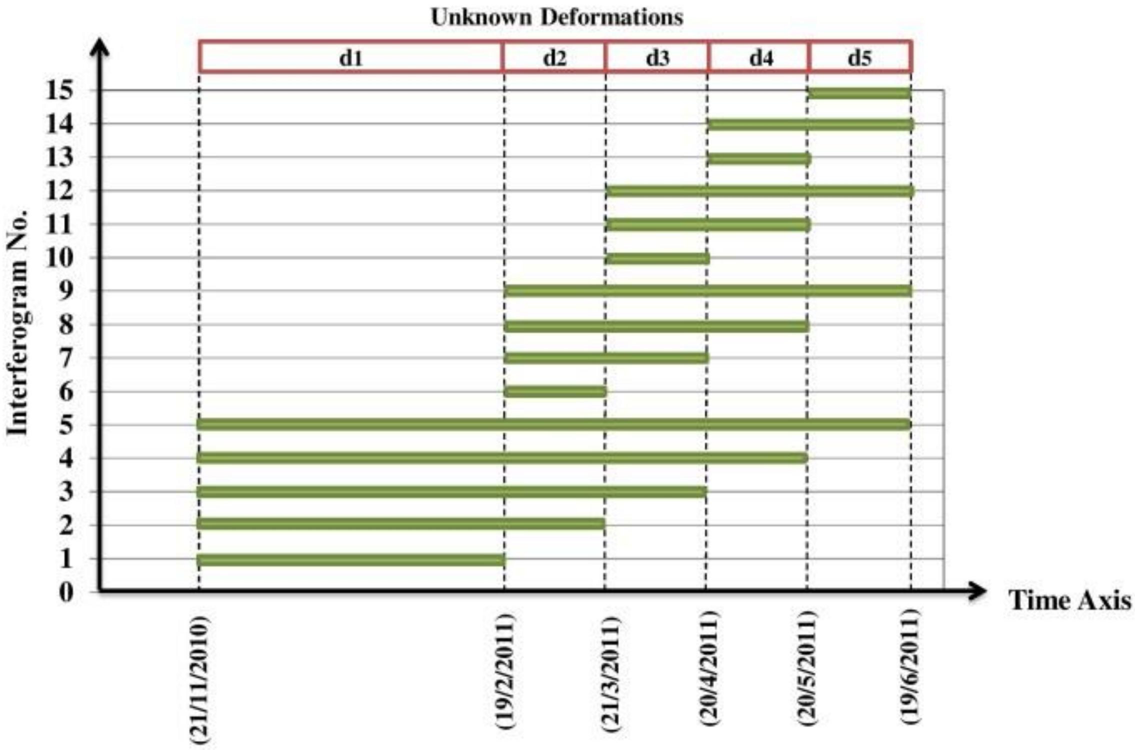

Fig.5. Interferograms stack structure, each bar represents an interferogram with the right end at the master image acquisition date and the left end at the slave image acquisition date.

Table 1

Details of SAR images and interferograms.

Master	Slave	No.	B⊥ (m.)	∆ t (days)	Satellite/Sensor /Direction
21 November 2010	19 February 2011	1	-245	90	ENVISAT-ASAR C-band Single polarization (HH) Descending Critical Normal Baseline (2100 m.)
	21 March 2011	2	-438	120	
	20April 2011	3	-458	150	
	20May 2011	4	415	180	
	19June 2011	5	-556	210	
19 February 2011	21 March 2011	6	-228	30	
	20April 2011	7	-218	60	
	20May 2011	8	244	90	
	19June 2011	9	-337	120	
21 March 2011	20April 2011	10	99	30	
	20May 2011	11	377	60	
	19June 2011	12	-127	90	
20April 2011	20May 2011	13	295	30	
	19June 2011	14	-127	60	
20May 2011	19June 2011	15	-416	30	

4.2 Analysis

The unwrapped phase maps for all of the interferograms were generated and referenced to GPS station no. 3025 as shown in (Fig. 1.b) (Fig. 3, Step A). Then, we analyzed the LOS deformation time series for this GPS station to estimate the best deformation trends (Fig. 4). We chose a combination of linear and power models as illustrated in section 3.2 (Fig. 3, Step B). In this analysis, we used only GPS station no. 3025 and left the other GPS stations for accuracy verifications. As shown in (Fig. 1.b), 17 GPS stations were identified within the study region; only eight GPS stations were located in pixels having a coherence value higher than the chosen threshold in the unwrapped phase stack. These eight GPS stations were chosen to verify the accuracy of the models used to present the deformation time series pattern. In Fig. 6, we present a comparison between the observed LOS deformations and the estimated deformation trend using the methodology presented in section 3.3.1 (Fig. 3, Step C) at seven GPS stations. This figure demonstrates the accuracy and reliability of the proposed models at most of the GPS stations, and because we use the raw unwrapped phase maps for modeling without any prior filtering, some GPS stations suffer from a constant shift value. For that reason, the main sequence of the proposed methodology is to correct the observed unwrapped phase maps first, and then re-estimate the deformation time series to avoid the leakage of modeling errors to the final estimated deformation values. The pixel containing GPS station no. 0226 exhibits a coherence value above the threshold for the whole unwrapped phase stack, but it suffered from large errors which prevented the convergence of the least squares system. Therefore, this pixel is not included in the presented results.

After estimating the parameters of each pixel, we used a moving 7-pixels-by-7-pixels window to interpolate the three model parameters for the un-estimated pixels that have reliable neighboring pixels within the 7-by-7 window, as shown in section 3.3.1. The parameters for GPS stations no. 3020, 3027, 3033, 3037, 0226 and 0756 were successfully retrieved.

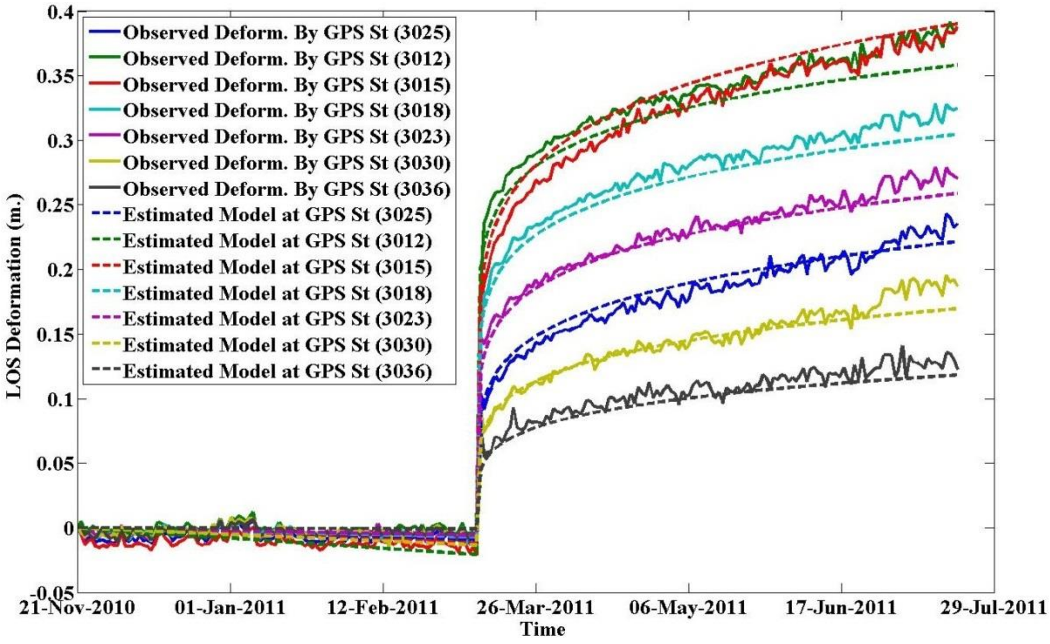

Fig.6. Observed LOS deformations and estimated deformation trends at GPS stations (descending direction).

The next analysis step, illustrated in section 3.3.2 and (Fig. 3, Step D), is to calculate the deformation values at the acquisition times of the SAR images and then construct deformation maps equivalent to the raw unwrapped phase maps in structure and number. After subtracting the estimated deformation trends from the raw unwrapped phase maps, the generated residual phase maps will be ready for temporal and spatial filtering.

We used the least squares method, illustrated in section 3.4.1, to filter the residual unwrapped phase maps temporally (Fig. 3, Step E). Then, we applied a ramp removal to every temporally filtered residual phase map to correct for the spatially correlated imposed errors, as described in section 3.4.2 (Fig. 3, Step F).

Finally, we restored the deformation trend to the filtered residual phase maps and used the final corrected unwrapped phase maps to estimate the deformation time series for the entire study region using least squares analysis, as illustrated in section 3.5 (Fig. 3, Step G). The final deformation and DEM error maps are presented in (Fig. 7).

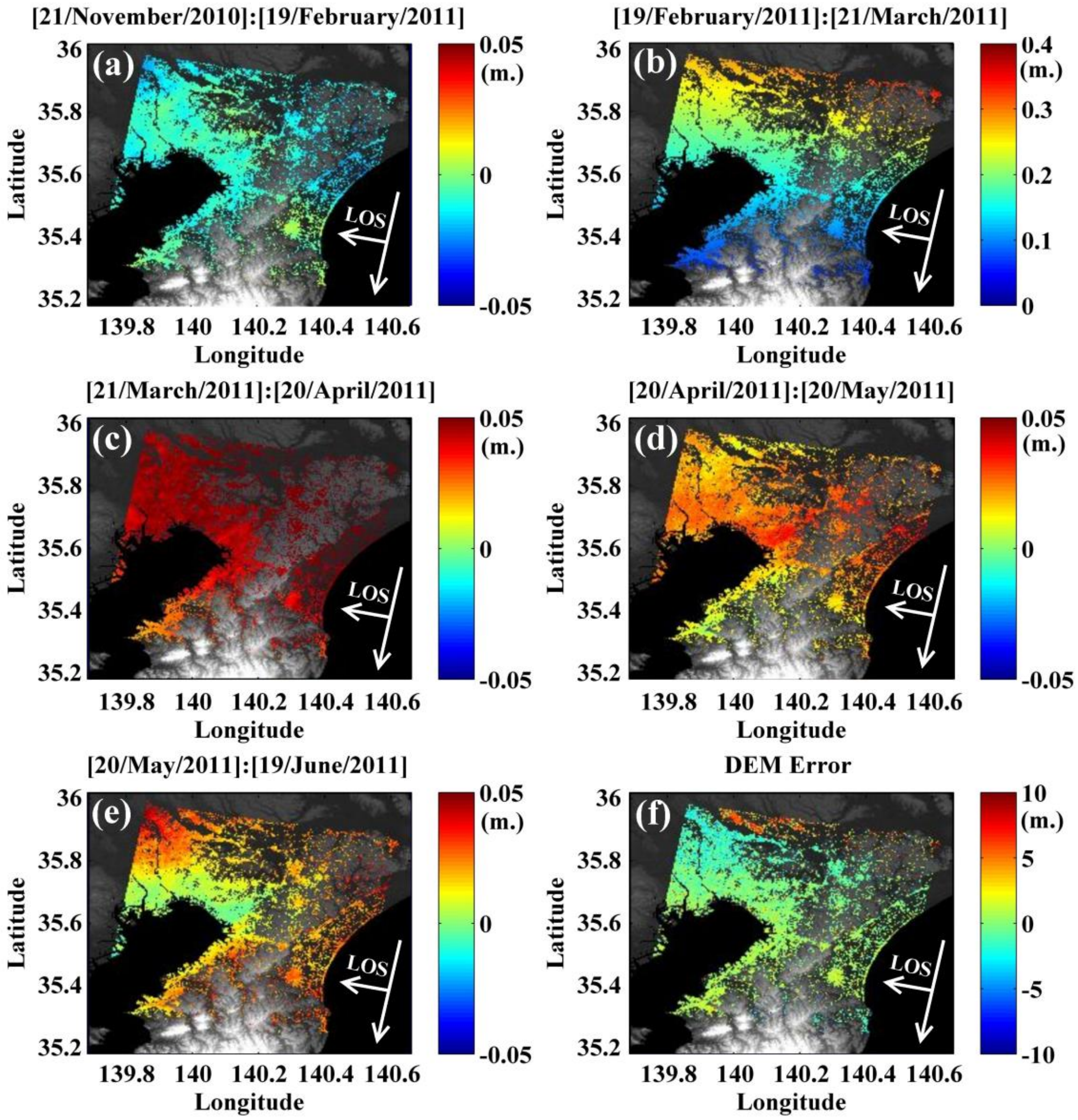

Fig.7. [a : e] Final deformation maps, [f] DEM error, background is a DEM map.

4.3 Accuracy Check

In the final deformation maps, deformation for only 13 out of 17 GPS stations was estimated (Fig. 1.b). Accuracy verification was performed by comparing the estimated LOS deformation values at those 13 GPS stations and GEONET's corrected coordinates (see Fig. 8, Fig. 9 and Fig. 10).

The descending LOS deformation time series for the 13 GPS stations are presented in Fig. 8. The solid lines show the daily deformation evolution observed by GEONET's GPS stations, while the circles represent the estimated deformation time series at the locations of GPS stations. The analysis method calculates a discrete epoch-to-epoch deformation map. Therefore, successive accumulation of the deformation values must be done first to estimate the deformation time series.

The errors in the discrete deformation maps at the locations of the 13 GPS stations are presented in Fig. 9. We found that the proposed methodology can effectively reduce the amount of errors and give a mean standard deviation and RMS error at the millimeter level (see table 2).

Another comparison between the estimated discrete deformation values at the 13 GPS stations and the observed deformation by GPS stations are presented in Fig. 10. The estimated correlation value equals 0.99, which demonstrates the accuracy and reliability of the proposed methodology, especially if we considered that the deformation presented in InSAR are the average values of all of the scatterers present in the pixel, while the deformation observed by the GPS represents only a single point with location accuracy on the sub-cm scale.

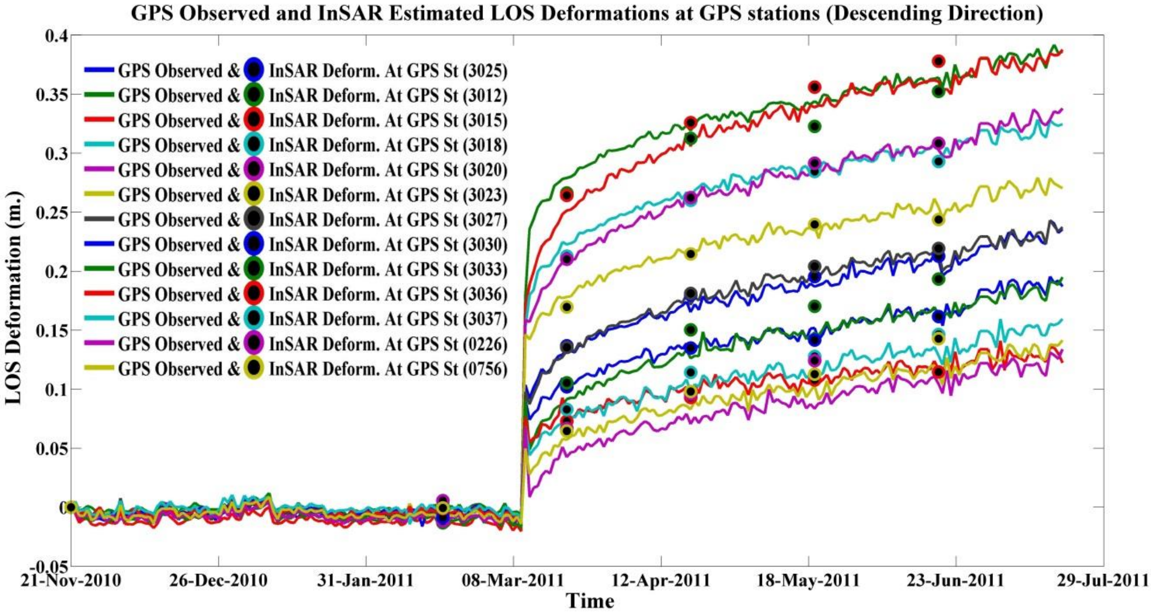

Fig.8. GPS observed deformations (solid lines) against InSAR estimated deformations (dots) in LOS descending direction at 13 GPS stations.

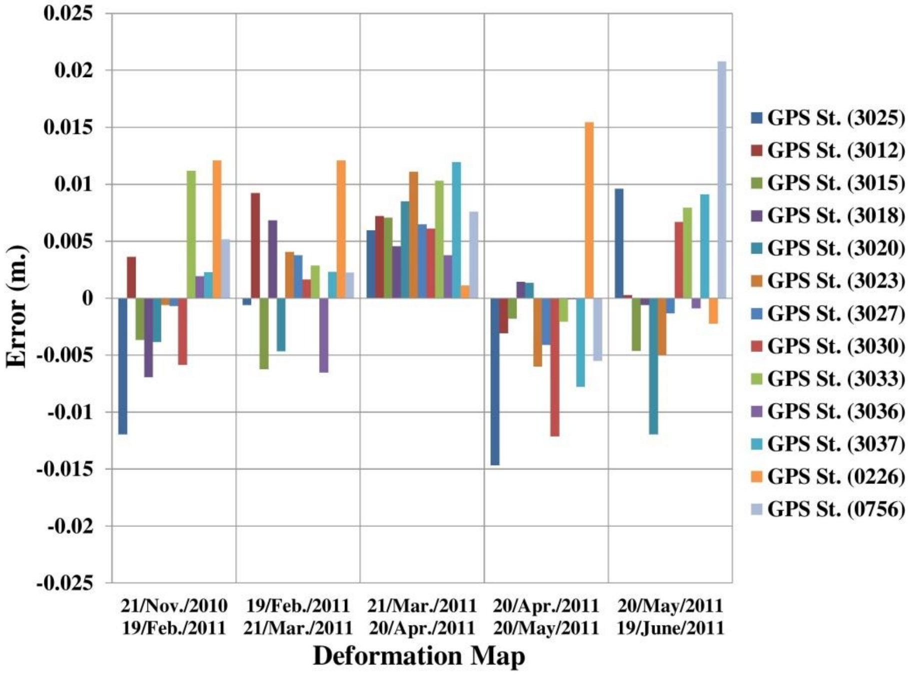

Fig.9. Deformation maps errors at GPS stations

Table 2

Statistical analysis results for GPS stations time series

GPS station ID	Error Standard Deviation (± mm.)	Error Mean Value (mm.)	RMS Error (± mm.)
3025	9.6	-2.3	9.9
3012	4.5	3.4	5.6
3015	4.7	-1.8	5.0
3018	4.7	1.1	4.9
3020	6.8	-2.1	7.1
3023	6.3	0.7	6.3
3027	3.8	0.8	3.9
3030	7.2	-0.7	7.3
3033	5.0	6.0	7.8
3036	3.5	-0.4	3.5
3037	6.8	3.6	7.7
0226	6.9	7.7	10.4
0756	8.6	6.1	10.5
Mean	6.0	1.7	6.9

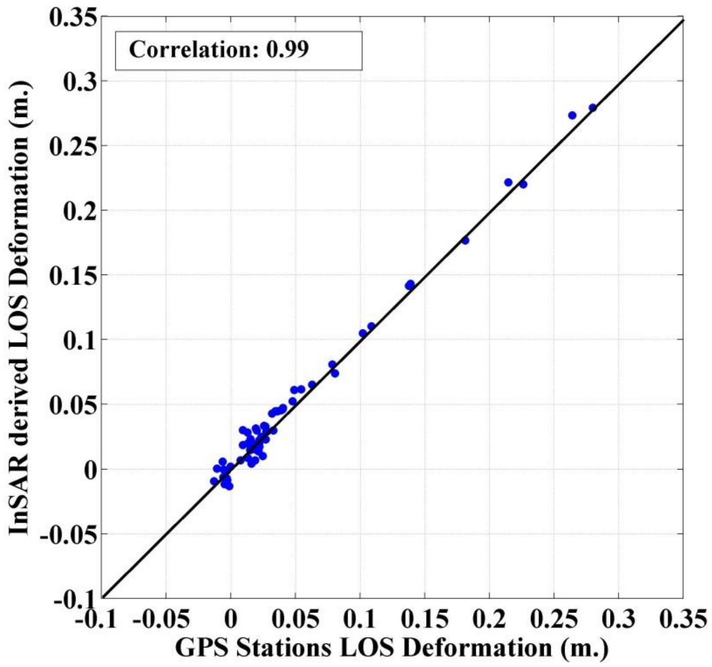

Fig.10. InSAR LOS deformations obtained by GPS against deformations obtained by InSAR

5. Discussion of Deformation Signature

This section introduces a brief discussion of the 2011 Tohoku earthquake's deformation signature. We chose to discuss two main categories of the deformation patterns based on the analysis presented in this paper. First, we introduce the estimated model parameters and discuss the postseismic deformation pattern in the Kanto region. Then, we introduce the effect of soil liquefaction, which resulted in severe local deformation, especially around the Tokyo bay area. Finally, we present the postseismic deformation for the areas that suffered from soil liquefaction.

5.1 Postseismic Deformation Pattern

We model the deformation signature of the Kanto region, Japan, using linear and power models (section 3.3.1). The linear model parameter [a] represents the mean velocity of the pixels during the three months before the 2011 Tohoku earthquake, which is nearly constant and negligible. On the other hand, the multiplication parameter [b] (Fig. 11, a) represents the main and sudden shock of the earthquake on March 11, 2011. This map shows the deformation in meters converted from the unwrapped phase maps to before modeling. It is clear that the instant shock intensity increases in the northeast direction, which is the location of the epicenter of the earthquake.

The power parameter [c] (Fig. 11, b) represents the inverse rate of decay of the postseismic deformation. This means, for large values of parameter [c], the postseismic deformation is expected to be large as well. This figure shows that the southern part of the study area experienced more postseismic deformation than in the north. This result suggests that the postseismic deformation in the Kanto region is subjected to activities other than the relaxation of the 2011 Tohoku earthquake rupture zone (Somerville, 2014).

For better understanding of this phenomenon, we present the postseismic deformation maps from April 20, 2011 to May 20, 2011 (Fig. 11, c) and from May 20, 2011 to June 19, 2011 (Fig. 11, d). These figures show that area "A" (Boso Peninsula) is subjected to an increase in the postseismic deformation starting from May 20th, 2011. To validate this observation, we calculated the ratio between the postseismic deformation and coseismic deformation before and after May 20th, 2011. In (Fig. 11, e), we present the ratio between the postseismic deformation from March 21, 2011 to May 20, 2011 to the coseismic deformation (February 19, 2011 to March 21, 2011). This figure shows that the postseismic deformation is less than the coseismic deformation in nearly the entire study area up to May 20th, 2011. In (Fig. 11, f), we present the ratio between the postseismic deformation from March 21, 2011 to June 19, 2011 to the coseismic deformation (February 19, 2011 to March 21, 2011). This figure shows that the postseismic deformation increased significantly in the southeast direction after May 20th, 2011. This postseismic deformation can be attributed to an activity in the Off Boso segment as a result of the large effect of the 2011 Tohoku earthquake. This postseismic activity may be one of the reasons for shortening the recurrence interval of Boso slip events (Ozawa, 2014). The off Boso slip events can be described as follows: because of the subduction of the Philippine Sea plate from the Sagami though, the Boso peninsula is moving in the northwest direction. However, GPS observed motion showed south-southeast movements in 1996, 2002, 2007 and 2011. These transients are interpreted to be caused by slow slip events in which the Okhotsk plate moves southeast in the plate interface, opposite the direction of the subducting Philippine Sea plate (Fig. 12) (Ozawa, 2014).

Another observation is the increase of postseismic deformation in area “B” (Fig. 11, d). This deformation can be justified by postseismic activity of the Kanto fragment. The Kanto fragment as suggested in (Toda et al., 2008) is a fragment of the pacific plate that has broken off and become lodged between the Pacific, Philippine Sea and Okhotsk plates, under Tokyo. It is suggested that most of Tokyo’s seismic behavior is attributed to the sliding of the fragment against the other tectonic plates (Fig. 12) (Toda et al., 2008).

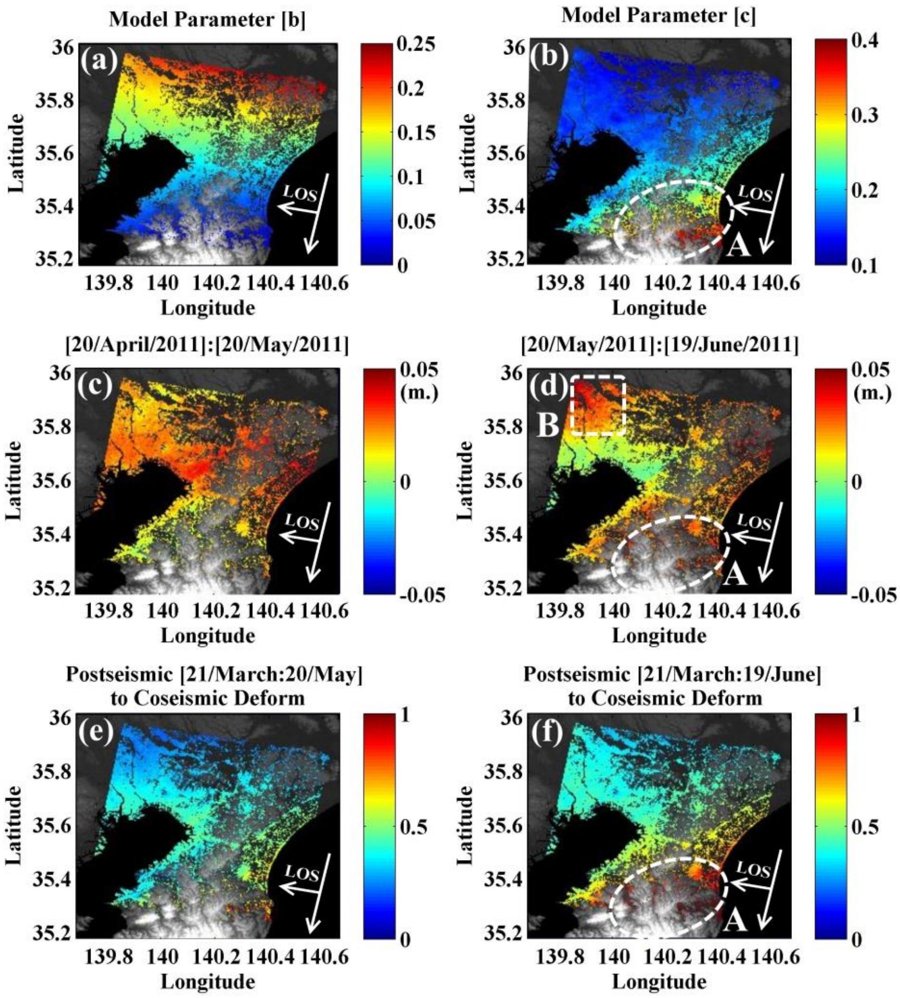

Fig. 11. (a) Multiplication model paramter [b], (b) power model paramter [c], (c) postseisimc deformation map [20/April/2011 : 20/May/2011],(d) postseisimc deformation map [20/May/2011 : 19/June/2011], (e) ratio between the postseisimc deformation up to May 20th, 2011 and the coseismic deformation, (f) ratio between the postseisimc deformation up to June 19th, 2011 and the coseismic deformation, background is a DEM map.

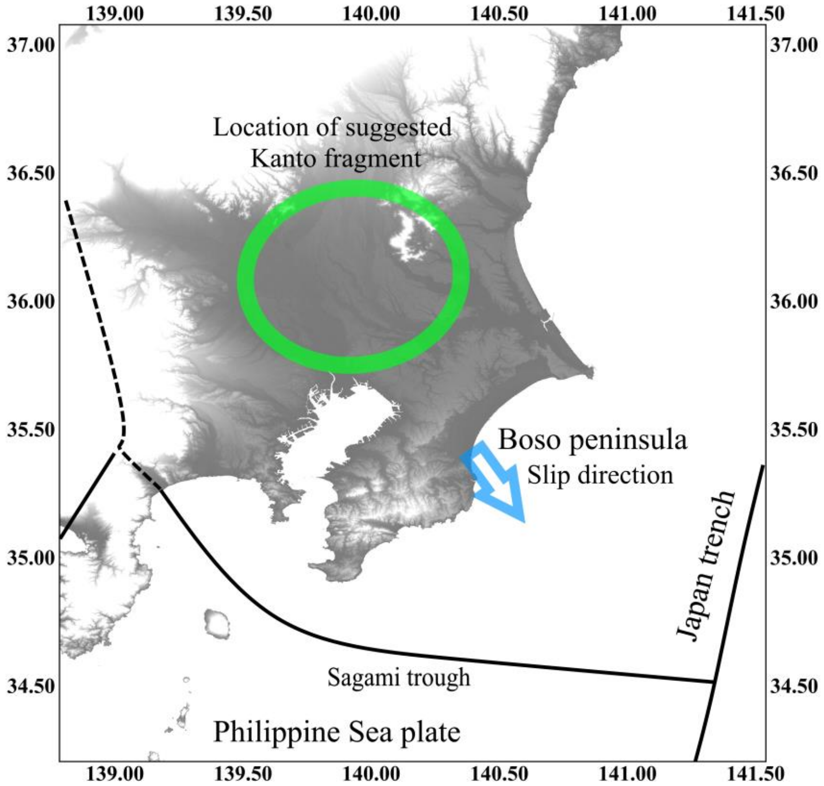

Fig. 12. Boso pensisula slip direction and the location of the suggested Kanto fragment

5.2 Local Deformation

This section presents the effect of local deformation in the study area, focusing on the Tokyo bay area, which suffered from severe damage due to soil liquefaction (Fig. 1.b).

5.2.1 Soil Liquefaction Identification

We are able to identify the pixels that have been affected by soil liquefaction. We use the coherence difference method presented by (Ishitsuka et al., 2012) and (Tamura and Li, 2013). The main idea of this approach is to identify the pixels that lost coherence as a result of a certain event. This can be done by subtracting a preseismic coherence map from the coseismic coherence map and setting a suitable threshold.

In this analysis, we subtract preseismic coherence map no. 1 from the coseismic coherence map no. 6 (Fig. 5). In the estimated coherence difference map, a zero value means no change in coherence, a negative value means decreased coherence and a positive value means increased coherence. Pixels suffering from soil liquefaction will exhibit coherence loss. To identify the pixels that are most likely affected by soil liquefaction, we use a threshold of $(< -\sigma)$ (Fig. 13, b), where (σ) is the standard deviation of the coherence difference map. We chose this threshold based on comparison of the results with the observed liquefaction map (Fig. 13, d) presented by the Kanto Regional Development Bureau of the Ministry of Land, Infrastructure, Transport and Tourism (KRDB) and the Japanese Geotechnical Society (JGS) (2011).

5.2.2 Postseismic Deformations For Uncorrelated Pixels

The damage due to soil liquefaction caused phase decorrelation for the affected areas in the coseismic interferograms (Fig. 5). This phase decorrelation prevents the estimation of postseismic deformation values for the affected areas using the proposed methodology (Fig. 13, a) mainly because most of the interferogram stack records the coseismic deformation from the 2011 Tohoku earthquake.

To solve this problem, we use the estimated postseismic deformation maps presented in this analysis to correct the errors in the raw postseismic unwrapped phase maps. First, we identify the three postseismic deformation maps from this analysis [21/March/2011]: [20/April/2011] (Fig. 7, c), [20/April/2011]: [20/May/2011] (Fig. 7, d) and [20/May/2011]: [19/June/2011] (Fig. 7, e). Then, we identify the corresponding postseismic unwrapped phase maps (No. 10, 13 and 15, respectively) (Fig. 5). By subtracting every deformation map from its corresponding unwrapped phase map, we will obtain an estimation of the imposed errors eq. (12).

$$Imposed\ Errors = Unwrapped\ phase\ map - estimated\ deformation\ model \qquad (12)$$

Then we use a 7-pixels-by-7-pixels moving window to interpolate the imposed errors in the decorrelated pixels. For this small window, the imposed errors are highly correlated spatially. Finally, we estimate the postseismic deformation maps by subtracting the interpolated error maps from the raw unwrapped phase maps (Fig. 13, c).

The final postseismic deformation map presented in (Fig. 13, c) is total deformation value from [21/March/2011] to [19/June/2011]. The areas suffering from soil liquefaction showed relatively smaller postseismic deformations compared to other neighboring areas.

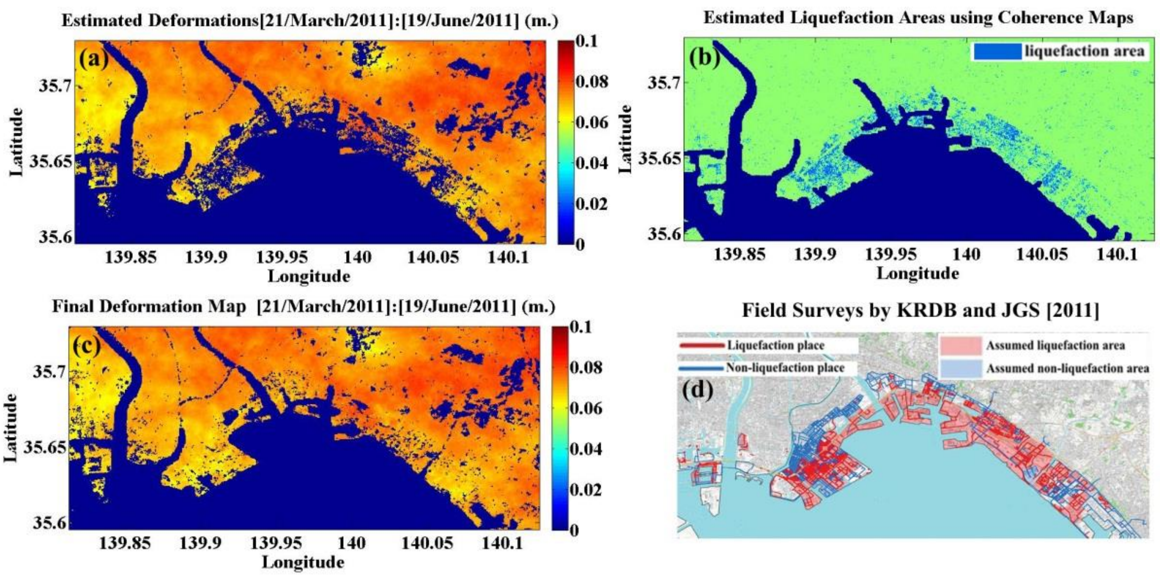

Fig. 13. (a) Postseismic deformation maps using the proposed method, (b) Liquefaction areas using the coherence difference method, (c) Final postseismic deformation maps,(d) Observed liquefaction through field surveys conducted by KRDB and JGS (2011).

6. Conclusions

The main aim of this paper is to estimate the coseismic and postseismic crustal deformation of the Kanto region, Japan, with geodetic accuracy. The study area was subjected to large deformation as a result of the 2011 Tohoku earthquake. Several challenges were identified during the analysis such as the large, uneven deformation that dominated the entire study area, leaving few stable zones to facilitate the identification of the imposed errors and the limited number of available coseismic and postseismic SAR images.

To overcome these challenges, we designed a methodology that uses the observed deformation from a single GPS station to determine the best deformation trends that describe the earthquake signature, then use a least squares solution for nonlinear multi-model parameter estimation. The estimated deformation trends are removed from the unwrapped phase maps to preserve the main deformation signature during the filtering processes implemented on the residual phase maps. Finally, the estimated deformation trends are restored to the filtered residual phase, and the final deformation estimation process is implemented.

The proposed methodology was tested using six C-band SAR images and a single GPS station. The GPS station was used to identify the best deformation trends and registering the unwrapped phase maps. The final estimated deformation maps were tested against the observations of 13 GPS stations and the mean values of the standard deviation error and RMS error were 6.0 and 6.9 mm, respectively. These results demonstrate the reliability and accuracy of the proposed methodology.

Furthermore, we include a brief discussion about the estimated deformation signatures in our study area. The postseismic deformation patterns were presented, and an increase in the post-seismic deformation in Boso peninsula region was identified starting from May 20th, 2011. This postseismic deformation can be attributed to activity in the Off Boso segment as a result of the effect of the 2011 Tohoku earthquake. In addition, the effects of local deformation due to soil liquefaction and local land subsidence were presented, focusing on the Tokyo bay area. The locations of soil liquefaction were identified, and their postseismic deformation was presented.

We believe that this method can be utilized to study complex and fine-scale surface deformations in areas that have been affected by large dominating deformation signatures and contain at least single GPS station.

Acknowledgment

We are grateful to the Geospatial Information Authority of Japan (GSI) for the GPS displacements used in this study, and to the European Space Agency for providing all the ENVISAT's related data. We acknowledge the Kanto Regional Development Bureau of the Ministry of Land, Infrastructure, Transport and Tourism (KRDB) and the Japanese Geotechnical Society (JGS) for providing soil liquefaction data.

References:

Burgmann, R., Rosen, P. A., & Fielding, E. J. (2000). SYNTHETIC APERTURE RADAR INTERFEROMETRY TO MEASURE EARTH'S SURFACE TOPOGRAPHY AND ITS DEFORMATION. Annual Review of Earth and Planetary Sciences, 169–209.

Berardino, P., Fornaro, G., Lanari, R., & Sansosti, E. (2002). A New Algorithm for Surface Deformation Monitoring Based on Small Baseline Differential SAR Interferograms.

IEEE TRANSACTIONS ON GEOSCIENCE AND REMOTE SENSING, 40, 2375-2383.

Bhattacharya, S., Hyodo, M., Goda, K., Tazoh, T., & Taylor, C. (2011). Liquefaction of soil in the Tokyo Bay area from the 2011 Tohoku (Japan) earthquake. Soil Dynamics and Earthquake Engineering, 1618–1628.

Biggs, J., Wright, T., Lu, Z., & Parsons, B. (2007). Multi-interferogram method for measuring interseismic deformation: Denali Fault, Alaska. Geophysical Journal International, 170(3), 1165–1179.

Buckley, S. M., Rosen, P., Hensley, S., & Tapley, B. (2003). Land subsidence in Houston, Texas, measured by radar interferometry. JOURNAL OF GEOPHYSICAL RESEARCH, VOL. 108, 8-1:8-12.

Costanthi, M., & Rosen, P. (1999). A Generalized Phase Unwrapping Approach for Sparse Data. Geoscience and Remote Sensing Symposium. 1, pp. 267 - 269. Hamburg: IEEE.

ElGharbawi, T., & Tamura, M. (2014, February). Measuring deformations using SAR interferometry and GPS observables with geodetic accuracy: Application to Tokyo, Japan. ISPRS Journal of Photogrammetry and Remote Sensing, 88, 156–165.

Feng, G., Ding, X., Li, Z., Mi, J., Zhang, L., & Omura, M. (2012). Calibration of an InSAR-Derived Coseimic Deformation Map Associated With the 2011 Mw-9.0 Tohoku-Oki Earthquake. IEEE GEOSCIENCE AND REMOTE SENSING LETTERS, 9(2), 302-306.

Goldstein, R. M., & Werner, C. L. (1998). Radar interferogram filtering for geophysical applications. GEOPHYSICAL RESEARCH LETTERS, 25(21), 4035-4038.

Goldstein, R. M., Engelhardt, H., Kamb, B., & Frolich, R. M. (1993). Satellite Radar Interferometry for Monitoring Ice Sheet Motion: Application to an Antarctic Ice Stream. SCIENCE, VOL.262, 1525-1530.

Gourmelen, N., Amelung, F., & Lanari, R. (2010). Interferometric synthetic aperture radar–GPS integration: Interseismic strain accumulation across the Hunter Mountain fault in the eastern California shear zone. Journal of Geophysical Research: Solid Earth, 115, B09408.

Imakiire, T., & Kobayashi, T. (2011). The Crustal Deformation and Fault Model of the 2011 off the Pacific Coast of Tohoku Earthquake. Bulletim of the Geospatial Information Authority of Japan, 59, 21-30.

Ishihara, K. (2012). LIQUEFACTION IN TOKYO BAY AND KANTO REGIONS IN THE 2011 GREAT EAST JAPAN EARTHQUAKE. International Symposium on Engineering Lessons Learned from the 2011 Great East Japan Earthquake, (pp. 63-81). Tokyo, Japan.

Ishitsuka, K., Tsuji, T., & Matsuoka, T. (2012). Detection and mapping of soil liquefaction in the 2011 Tohoku earthquake using SAR interferometry. Earth Planets Space, 1267–1276.

Kanto Regional Development Bureau of Ministry of Land, I. (2011). Investigation of soil liquefaction in Kanto region associated. (http://www.ktr.mlit.go.jp/) or (http://www.jiban.or.jp/) (in Japanese).

Martinez, N. Y., Eineder, M., Cong, X. Y., & Minet, C. (2012). Ground Displacement Measurement by TerraSAR-X Image Correlation: The 2011 Tohoku-Oki Earthquake. IEEE GEOSCIENCE AND REMOTE SENSING LETTERS, 9(4), 539-543.

Massonnet, D., Feigl, K., Marc, R., & Adragna, F. (1994). Radar interferometric mapping of deformation in the year after the Landers earthquake. Nature, VOL. 369, 227-230.

Ozawa, S. (2014). Shortening of recurrence interval of Boso slow slip events in Japan. Geophysical Research Letters, Vol. 41(No. 8), 2762-2768.

Samsonov, S., Tiampo, K., Rundle, J., & Li, Z. (2007). Application of DInSAR-GPS Optimization for Derivation of Fine-Scale Surface Motion Maps of Southern California. IEEE TRANSACTIONS ON GEOSCIENCE AND REMOTE SENSING, 45, 512-521.

Sandwell, D., & Price, E. (1998). Phase gradient approach to stacking interferograms. JOURNAL OF GEOPHYSICAL RESEARCH, 103, 30,183-30,204.

Schmidt, D., & Bürgmann, R. (2003). Time-dependent land uplift and subsidence in the Santa Clara valley, California, from a large interferometric synthetic aperture radar data set. Journal of Geophysical Research: Solid Earth, 108, ETG 4.

Somerville, P. G. (2014). A post-Tohoku earthquake review of earthquake probabilities in the Southern Kanto District, Japan. Geoscience Letters, 1:10.

Tamura, M., & Li, W. (2013). Detection of Soil Liquefaction Areas in the Kantou Region using Multi-temporal InSAR Coherence. Asia-Pacific Conference on Synthetic Aperture Radar, (p. TH3.R1.3). Tsukuba, Japan.

Toda, S., Stein, R. S., Kirby, S. H., & Bozkurt, S. B. (2008). A slab fragment wedged under Tokyo and its tectonic and seismic implications. Nature Geoscience, 771 - 776.

Tokimatsu, K., Tamura, S., Suzuki, H., & Katsumata, K. (2012). Building damage associated with geotechnical problems in the 2011 Tohoku Pacific Earthquake. Soils and Foundations, 956–974.

Tong, X., Sandwell, D. T., & Smith-Konter, B. (2013). High-resolution interseismic velocity data along the San Andreas Fault from GPS and InSAR. JOURNAL OF GEOPHYSICAL RESEARCH: SOLID EARTH, 118, 369–389.

Tsukamoto, Y., Kawabe, S., & Kokusho, T. (2012). Soil liquefaction observed at the lower stream of Tonegawa river during the 2011 off the Pacific Coast of Tohoku Earthquake. Soils and Foundations, 987–999.

Wei, M., Sandwell, D., & Smith-Konter, B. (2010). Optimal combination of InSAR and GPS for measuring interseismic crustal deformation. Advances in Space Research, 46(2), 236–249.

Wright, T., Parsons, B., England, P., & Fielding, E. (2004). InSAR observations of low slip rates on the major faults of western Tibet. SCIENCE, 305, 236-239.

Yamagiwa, A., Hatanaka, Y., Yutsudo, T., & Miyahara, B. (2006, March). Real-time capability of GEONET system and its application to crust monitoring. Bulletin of the Geogrephical Survey Institute, 27-33.

Yamaguchi, A., Mori, T., Kazama, M., & Yoshida, N. (2012). Liquefaction in Tohoku district during the 2011 off the Pacific Coast of Tohoku Earthquake. Soils and Foundations, 811–829.

Yasuda, S., Harada, K., Ishikawa, K., & Kanemaru, Y. (2012). Characteristics of liquefaction in Tokyo Bay area by the 2011 Great East Japan Earthquake. Soils and Foundations, 793–810.

Zhang, S., Li, T., Liu, J., & Xia, Y. (2008). Research on the Linear and Nonlinear Methods of Correcting Baseline Errors on SAR Interferograms. The International Archives of the Photogrammetry, Remote Sensing and Spatial Information Sciences., 161-164.